Cost-effective (non-contact) ultrasound system for bearing fault diagnostics: Development, Validation and Benchmark

Agusmian Partogi OMPUSUNGGU[1], Maarten SPRENGERS[2], and Theodor Andrei BARTIC[1]

[1]Flanders Make vzw
Celestijnenlaan 300, B-3001 Leuven, Belgium
agusmian.ompusunggu@flandersmake.be

[2] KU Leuven, Technology Cluster Mechanical Engineering
Kleinhoefstraat 4, 2440 Geel, Belgium

Abstract

Contact sensors (e.g. accelerometer) have been widely used for vibration-based bearing fault diagnostics. However, in applications where the use of contact sensors is not possible, a non-contact sensor (e.g. ultrasound sensor) is a must. Besides achieving the desired functionality, namely being sensitive for fault detection, the solution should also be cost-effective. In this paper, the development of a cost-effective ultrasound system for bearing fault diagnostics is presented. The developed system was tested and benchmarked against a high-end accelerometer and a high-end acoustic emission sensor on an industrially representative gearbox setup that can emulate either healthy or faulty state under different operating conditions. The benchmark analysis shows that the three sensors provide comparable diagnostics performance for shaft speeds higher than 500 rpm.

1 Introduction

Rolling element bearings are one of critical components often reported as the major cause of total breakdowns in industrial rotating machinery. Since unexpected breakdowns might lead to long downtimes (i.e. production loss) and eventually result in high costs, a condition monitoring system that can provide the actual status of a bearing is desirable to avoid such undesired events. Bearing condition monitoring based on vibration measurement is widely applied in industrial applications and the signal processing techniques have been matured [1]. In this regard, vibration signals are typically measured using accelerometers mounted on the structure of the machines, e.g. bearing housing. In some applications, however, mounting a sensor on the machine structure is not possible due to the design or operation constraints, e.g. additional mass is not allowed, or no space is available for sensor mounting. Therefore, a bearing condition monitoring system based on a non-contact sensing technique is desired for such situations.

As reported in Refs. [2,3], a broadband capacitive (non-contact) air-coupled ultrasound sensor (ACUS) has shown some potential to be used for bearing faults diagnostics. Various signal processing techniques were applied to extract diagnostic information (i.e. features) from ultrasound signals and it was shown that wavelet-based features give the best diagnostic performance. However, the total price of the ACUS and the amplifier used in Refs. [2,3] is still relatively high for practical applications, which is of $5,930 (i.e. $1,980 for the sensor and $3,950 for the amplifier).

To remedy the gap of the use of ACUS for industrially relevant applications, a low-cost ACUS has been developed in this study. We have experimentally tested the developed ACUS on an industrially representative gearbox at different operating conditions. As a benchmark, we also mounted high-end accelerometers (ACC) and a high-end acoustic emission sensor (AES) to measure the dynamic response of the gearbox. All the signals were acquired simultaneously and then processed for extracting some diagnostic features. The diagnostic performances of the three sensors are then qualitatively compared.

2 Development of low-cost ultrasound system

2.1 Market survey, sensor selection and assembly

After a thorough market study, the ultrasound sensing element of PROWAVE 400EP250 was selected because of low-cost, good performance and having suitable properties for bearing fault diagnostics. The unit price of the sensing element is of 13.22 Euro. Note that the unit cost decreases to 9.65 Euro for ordering a large volume of 200 pieces. As shown in Figure 1, the resonant frequency of the sensing element is of 40 kHz with the bandwidth of 2 kHz around the resonance.

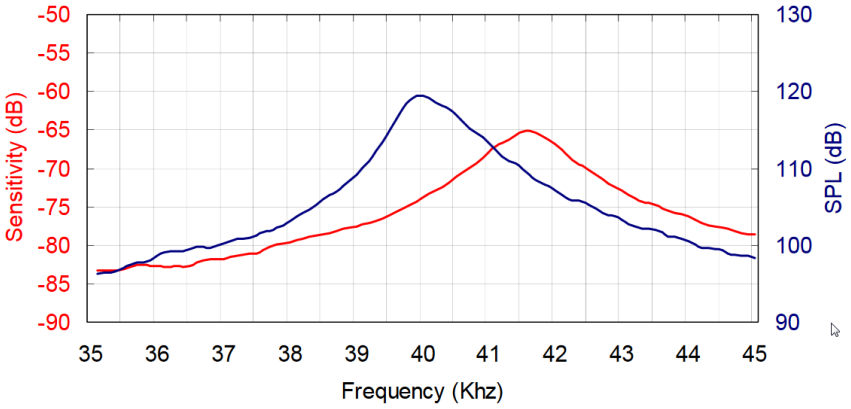

Figure 1: The frequency response of sensitivity/sound pressure level (SPL) of the sensor tested under 10 Vrms @30 cm (Taken from the datasheet).

Since the envisaged sensor system is expected to be used in industrial environments, therefore it should be robust against any external interferences, like electromagnetic interference (EMI). Moreover, the sensor usage and installation should also be straightforward for practical implementations. To this end, a sensor housing made of aluminium has been designed, tailored and manufactured. To ensure the sensing element to remain in its place and to allow proper grounding between the sensing element and the housing, a conductive glue is applied. Figure 2 shows the CAD model and the photo of the sensor system after the final assembly.

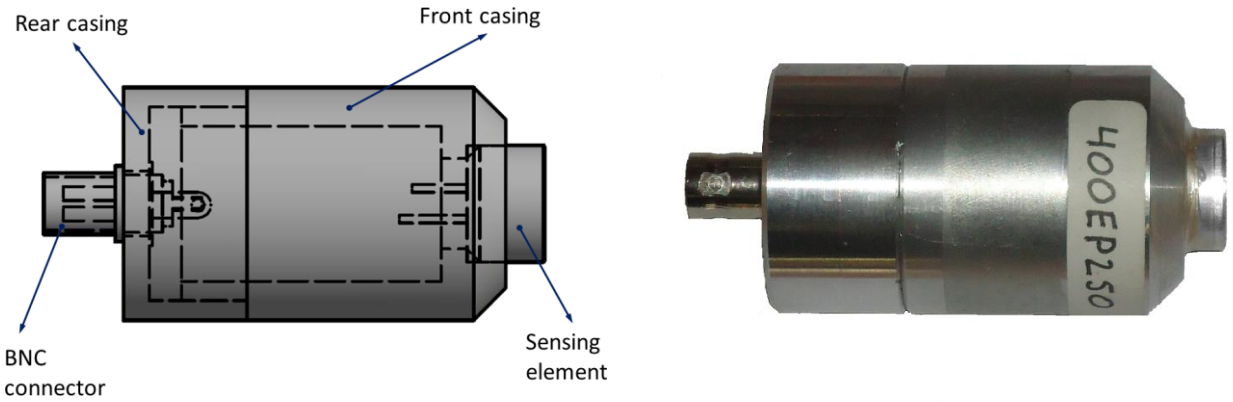

(a) (b)

Figure 2: The developed low-cost ultrasound sensor; CAD model (a), photo after assembly (b).

2.2 Amplifier

The signal obtained directly from the ultrasound sensor is rather weak, which is about 1 to 20 microvolts. Hence, the signal needs to be amplified by an analog amplifier prior to digitization in order to increase the signal-to-noise ratio (SNR), so useful information can be retrieved. For this purpose, an amplifier tailored for the ultrasound sensor was designed based on two low voltage audio amplifiers LM386 [4]. This amplifier type was selected because of simple design and low-cost. The developed amplifier has two-level amplification as schematically shown in Figure 3, where the amplification gain of each level is about 31.6. Thus, the total amplification gain of the amplifier is about 1000 times (~ 60 dB).

The amplifier has been made (all was done manually) and evaluated experimentally. The frequency response between the input and output channel has been measured as shown in Figure 4. It is seen in the figure that the amplification factor at 40 kHz, that matches to the sensor resonance frequency, is around 56 dB.

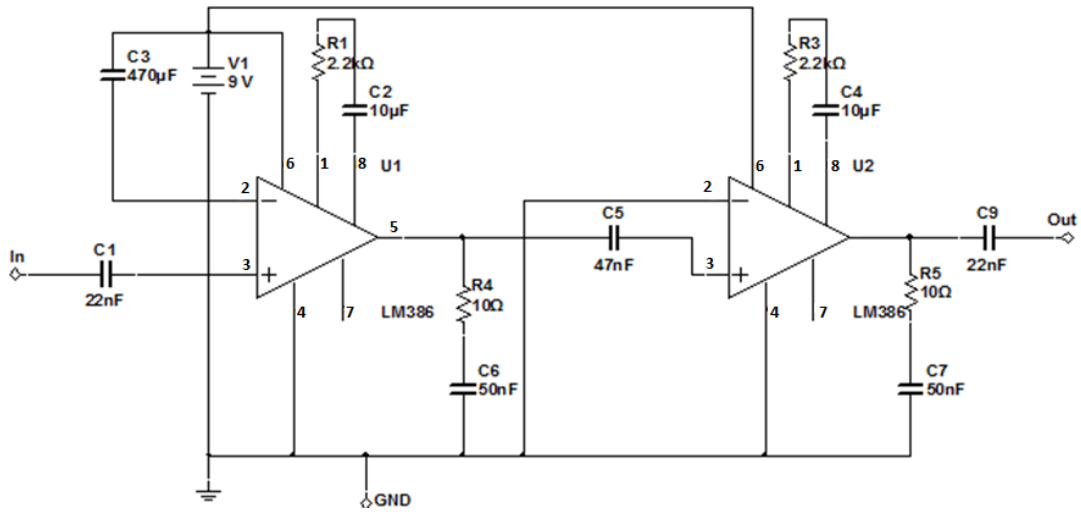

Figure 3: Schema of the amplifier.

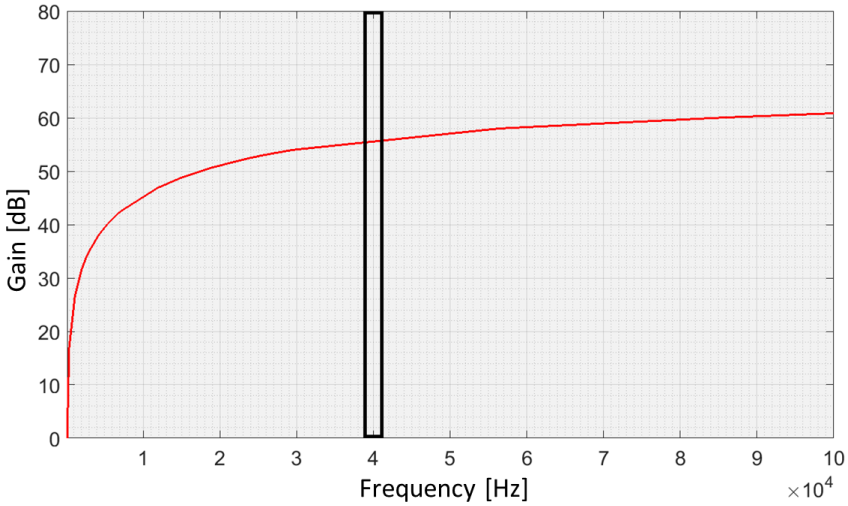

Figure 4: The measured frequency response of the amplifier obtained by using a sweep-sine input signal.

2.3 Cost analysis

The total cost estimation of the developed ultrasound system is summarized in Table 1. Notice that all listed prices are determined based on the assumption of a large volume production (e.g. 200 pieces).

Table 1: Cost analysis per system unit

Material	Price in Euro
Sensing element	10
Housing + BNC connector	18
Circuit board for amplifier + casing	12
Man-hour for assembly	10
Total	50

3 Experiment

3.1 Description of gearbox test setup

Figure 5 and Figure 6 respectively show the photograph and the layout of the gearbox test setup used in this study. The setup mainly consists of a parallel-gearbox (9), a bevel-gearbox (12), a magnetic brake to apply the load (10) and an induction motor to control the input shaft speed (4). Some details of the gears assembled in the two gearboxes are summarised in Table 2. Faulty and healthy machine elements, like rolling element bearings and gears, can be introduced on this test setup.

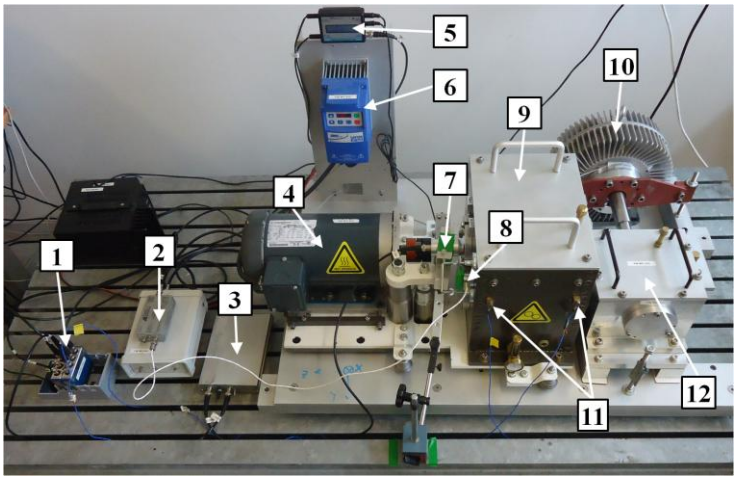

Figure 5: The gearbox test setup photograph; NI DAC system (1), amplifiers of the acoustic emission sensor (2), amplifier of the low-cost air-coupled ultrasound sensor (3), AC motor (4), tachometer (5), variable frequency drive (6), low-cost ultrasound sensor (7), high-end acoustic emission sensor (8), parallel-gearbox (9), magnetic brake (10), high-end accelerometers (11), bevel-gearbox (12).

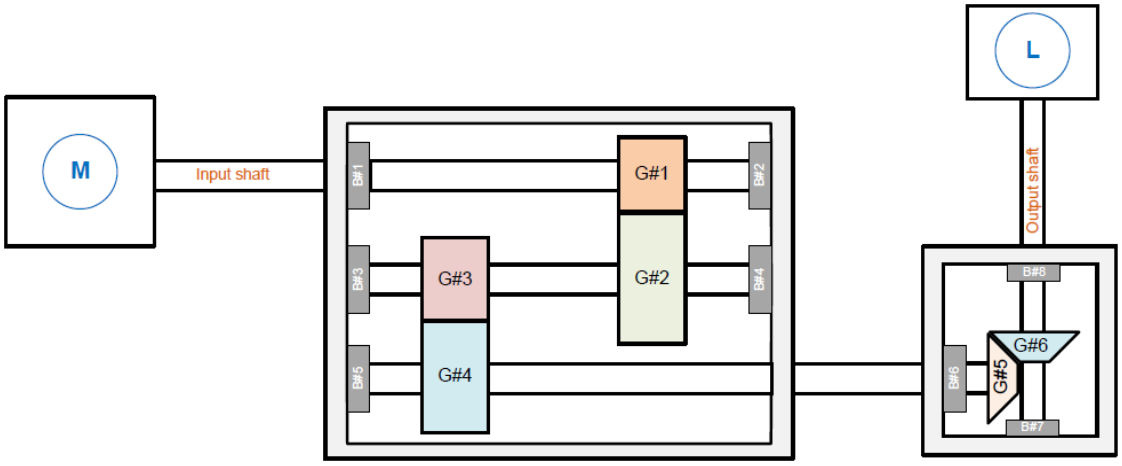

Figure 6: The gearbox layout.

Table 2: Gear overview

<table>
<tr><th>Gear</th><th>Number of teeth</th><th colspan="3">Gear ratio</th></tr>
<tr><td>G#1</td><td>29</td><td rowspan="2">3.448</td><td rowspan="3">8.621</td><td rowspan="5">17.24</td></tr>
<tr><td>G#2</td><td>100</td></tr>
<tr><td>G#3</td><td>36</td><td rowspan="2">2.500</td></tr>
<tr><td>G#4</td><td>90</td></tr>
<tr><td>G#5</td><td>20</td><td colspan="2" rowspan="2">2.000</td></tr>
<tr><td>G#6</td><td>40</td></tr>
</table>

3.2 Test procedure

In this study, two faulty bearings with different localized defect types, namely (*i*) *ball defect* and (*ii*) *inner race defect*, are considered. These bearings are ball bearing type (MB ER-16K) with the characteristic fault frequencies listed in Table 3.

Table 3: The characteristic bearing fault frequencies with f_r denoting the shaft speed in Hz.

Fault frequency	Hz
FTF	$0.402 \times f_r$
BPFO	$3.572 \times f_r$
BDF	$4.644 \times f_r$
BPFI	$5.430 \times f_r$

To simulate a faulty state, one of the defective bearings was mounted on the second shaft in the drive-end side of the parallel gearbox (indicated by B#3 in Figure 6). The gearbox setup was run under eight different operating conditions, with four different input shaft speeds (600, 1800, 2400 and 3000 rpm) and two different brake loads of 6 Nm (L1) and 20 Nm (L2). Because of the gear kinematics, the second shaft speed is 3.448 times lower than the input shaft speed, see Table 2. Hence, these input shaft speeds respectively correspond to 174, 522, 696 and 870 rpm on the second shaft, on which the faulty bearings were placed.

Three different vibro-acoustic sensors, namely a high-end accelerometer (ACC), a high-end acoustic emission sensor (AES) and the low-cost ultrasound sensor (ACUS) described in the previous section, were placed on different locations as indicated in Figure 5. The ACC is an ICP type sensor with the frequency range of 10 Hz to 10 kHz. The AES is the R6D type from Physical Acoustics that has a frequency range of 10 to 100 kHz. To minimize any ambient noise effect, the ACUS was placed about 5 mm from the bearing housing. An optical encoder was used to measure the input shaft rotational speed. All the signals are synchronously acquired by an NI DAQ system when the shaft speed is (quasi)-stationary and then stored to the PC with a Labview program. The ACC signal is sampled at 51.2 kHz, while both the AES and ACUS signals are sampled at 1 MHz.

4 Data processing methodology

For the performance comparison of the vibro-acoustic sensors in bearing fault detection and diagnosis, the envelope analysis based on the high frequency resonance technique (HFRT) is used [5]. As graphically shown in Figure 7, in this technique, the vibro-acoustic signal is first band-pass filtered around a certain frequency band of interest. For the ACC, the frequency band of interest is selected based on the resonance frequency excited in the transmission path between the fault location and sensor location. Nowadays, some tools for determining the frequency band of interest from measured vibration signals, like Kurtogram [6] and its variants, have become available. For both the AES and ACUS, the frequency band of interest is selected around the sensor resonance as specified by the sensor manufacturer (see Figure 1 for the ACUS sensor). For the AES, the elastic wave produced by the bearing fault is believed to propagate in the solid structure that eventually excites the AES resonance. For the ACUS, as a non-contact sensor, the sound wave generated by the bearing fault propagates through the air that eventually excites the ACUS resonance.

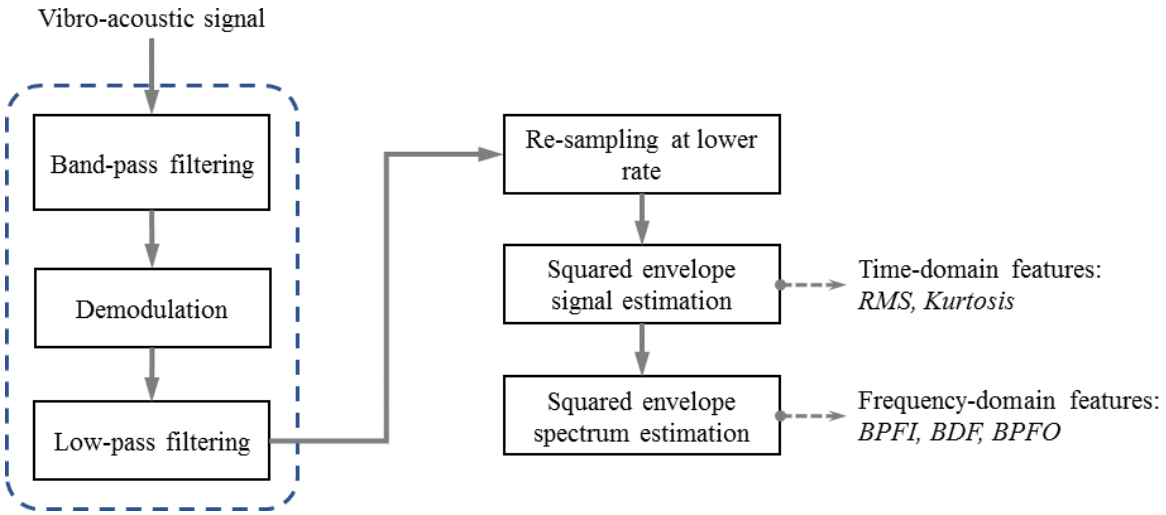

Figure 7: Block diagram of the signal processing and feature extraction, adapted from [5].

After band-pass filtering, the filtered signal is demodulated at the centre of the selected frequency band. The demodulated signal is then low-pass filtered with the cut-off frequency of half of the bandwidth of the frequency band to remove high frequency noise. Subsequently, the low-pass filtered signal is decimated at a lower sampling rate to gain computation time. As described in [1], the pseudo-periodic impulsive signature of bearing fault signals is enhanced by the squared envelope signal.

For quantitative comparison, number of features in the time-domain like the root-mean-square (RMS) and kurtosis are extracted from the squared envelope signal; meanwhile number of features in the frequency-domain, namely the weighted-mean magnitudes at the theoretical fault frequency (BPFI, BDF and BPFO) and the five harmonics, are extracted from the squared envelope spectrum. Here, the time-domain features are for fault detection, while the frequency-domain features are for fault diagnosis.

5 Results and discussion

Figure 8 until Figure 10 show the representative raw signals and the envelope signals for all the sensors and states at the *shaft speed 870 rpm* and *brake load 20 Nm*. Note that the envelope signals are estimated using the signal processing procedure shown in Figure 7.

It is seen in Figure 8(i) that the ACC signal in the *healthy state* is dominated by the periodic components originating from the gear dynamics, while the random patterns are more pronounced in the AES and ACUS signals, as shown in Figure 8(iii) and (v). Notably, the envelope signals estimated from the three sensor signals shown in Figure 8(ii), (iv) and (vi) do not show any impulsive (periodic) pattern, as expected for the healthy state.

In the defective rolling element case, it is still hard to see any periodic impact pattern due to the defect in both the raw ACC signal and the raw ACUS signal, see Figure 9(i) and (v). On the contrary, the periodic impact pattern is already evident in the raw AES signal as seen Figure 9(iii). After applying the signal processing technique to the three sensor signals, the periodic impact pattern becomes obvious as shown in Figure 9(ii), (iv) and (vi). As expected, the impact period T_{BD} is inversely proportional to the theoretical ball damage frequency ($T_{BD} = 1/BDF \approx 0.015$ s). Notably, the impact onsets detected by the AES and ACUS, as revealed in the envelope signals (see Figure 9(iv) and Figure 9(vi)), are quite the same. However, the impact onsets detected by the AES and ACUS differ from the impact onset detected by the ACC as revealed in the envelope signal Figure 9(ii).

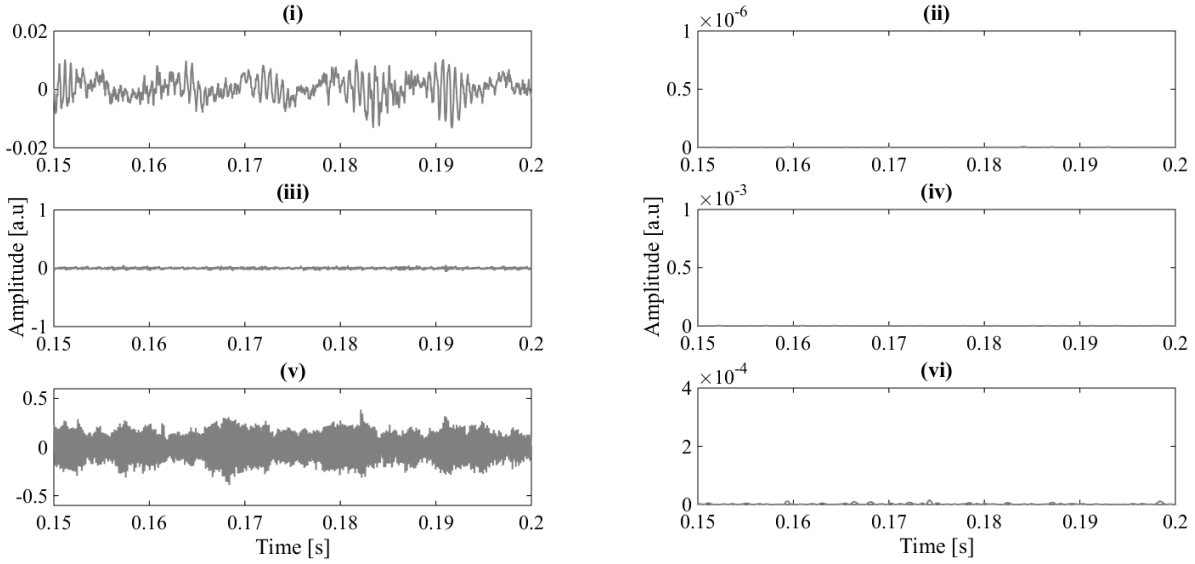

Figure 8: Signals in the *healthy gearbox state*: (i), (ii) the raw and the squared envelope signal of the ACC respectively; (iii), (iv) the raw and the squared envelope signal of the AES respectively; (v), (vi) the raw and the squared envelope signal of the ACUS respectively.

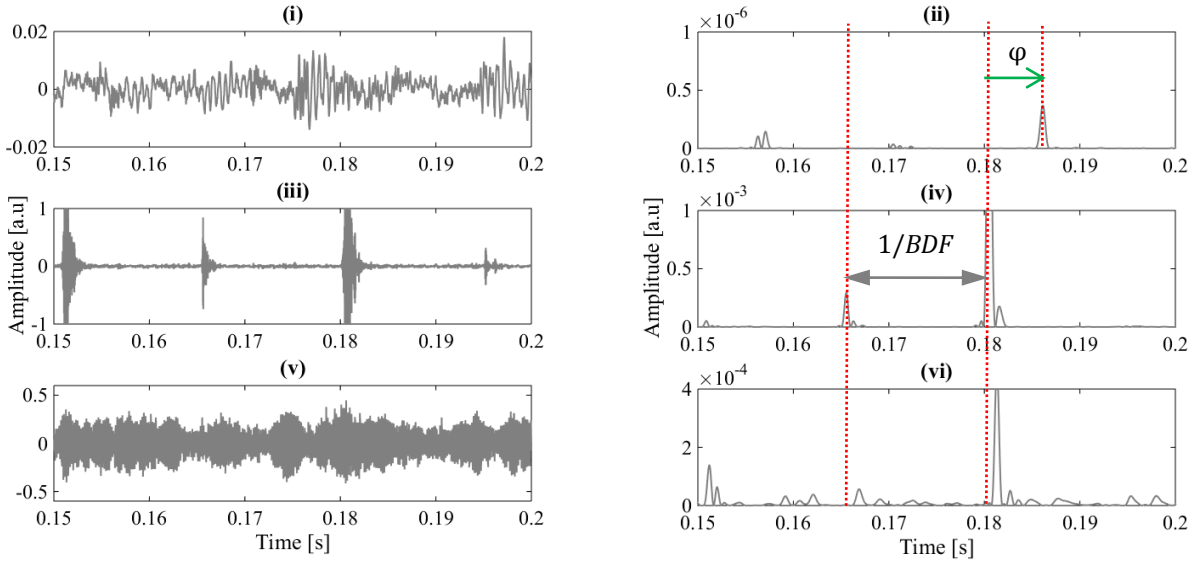

Figure 9: Signals in the *faulty gearbox state*, i.e. the presence of defective rolling element: (i), (ii) the raw and the squared envelope signal of the ACC respectively; (iii), (iv) the raw and the squared envelope signal of the AES respectively; (v), (vi) the raw and the squared envelope signal of the ACUS respectively.

Like the preceding case, a periodic impact pattern due to the inner race fault is already evident in the raw AES signal, see Figure 10(iii). In contrast, the periodic impact pattern due to the inner race fault is not well pronounced in the raw signals of the ACC and ACUS. After applying the signal processing method in Figure 7, the periodic impact pattern is clearly exposed in the envelope signals of the three sensors. As expected, the impact period T_{IRD} is inversely proportional to the theoretical inner race defect frequency (T_{IRD} = *1/BPFI* ≈ 0.013 s). Notably, the impact onsets detected by the three sensors are approximately at the same time instant, as revealed in the envelope signals shown in Figure 10(ii), (iv) and (vi).

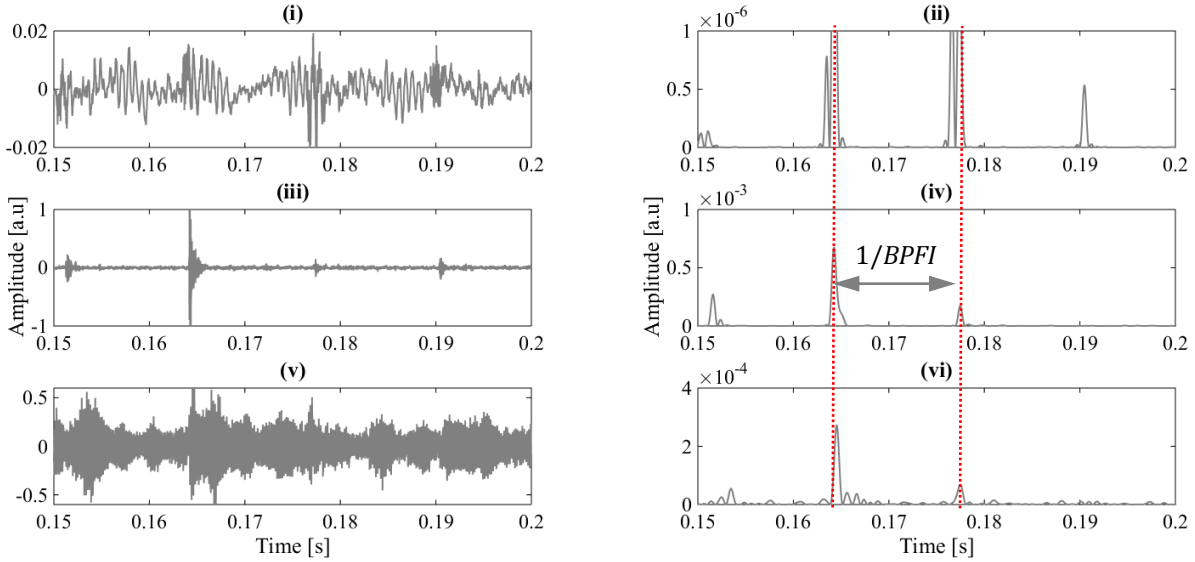

Figure 10: Signals in the *faulty gearbox state*, i.e. the presence of defective inner raceway: (i), (ii) the raw and the squared envelope signal of the ACC respectively; (iii), (iv) the raw and the squared envelope signal of the AES respectively; (v), (vi) the raw and the squared envelope signal of the ACUS respectively.

Figure 11-Figure 13 show the squared envelope spectra (SES) of all the sensors in all states. As a guidance, three dashed-lines indicating the theoretical fault frequencies (BPFO, BDF and BPFI) are also added in the graphs.

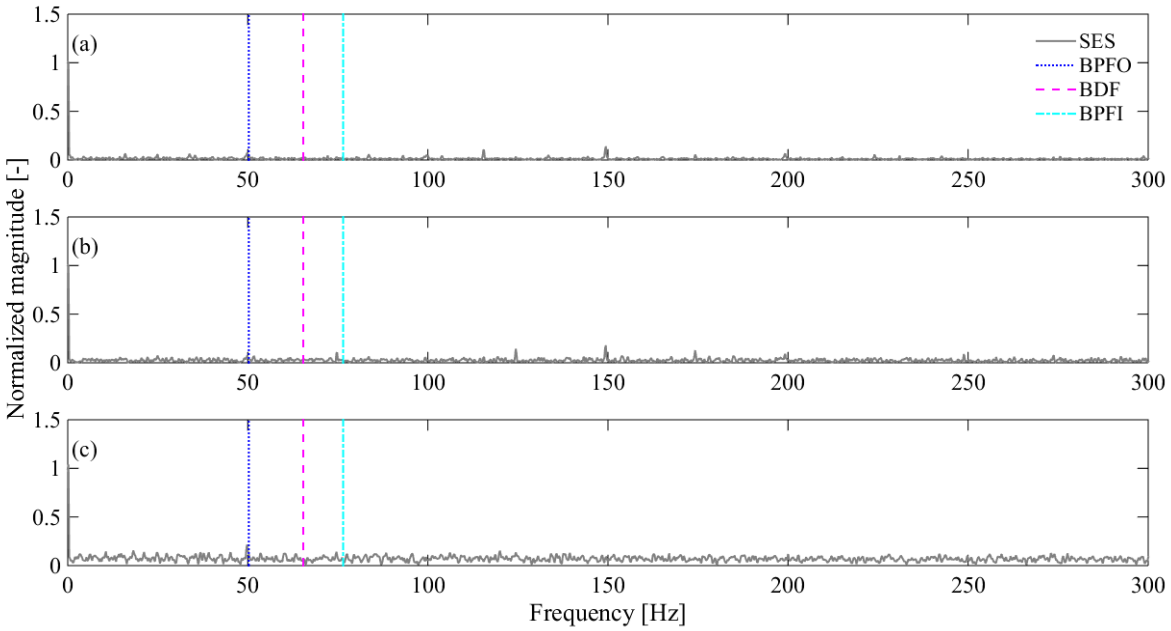

Figure 11: The squared envelope spectra (SES) obtained from the ACC signal (a), the AE signal (b) and the ACUS signal (c), in the *healthy gearbox state*.

As expected in the healthy case, no-peaks can be observed around the theoretical fault frequencies (BPFO, BDF and BPFI) in the SES of the three sensors, see Figure 11. In the defective rolling element case, peaks around the theoretical BDF and the harmonics are clearly exposed in the SES of the three sensors as shown in Figure 12. For a rolling element defect, some sidebands around the BDF and the harmonics that are spaced at the fundamental train frequency (FTF) are expected [1]. However, the sidebands are only exposed by the ACUS as shown in Figure 12(c). For the defective inner race case, peaks around the BPFI and the harmonics in the SES are clearly exposed in the SES of the three sensors, see Figure 13. Theoretically, some

sidebands around the BPFI that are spaced at the shaft frequency are also expected signature in the presence of an inner race defect [1]. The latter figure shows the evidence of the sidebands in the SES of the three sensors.

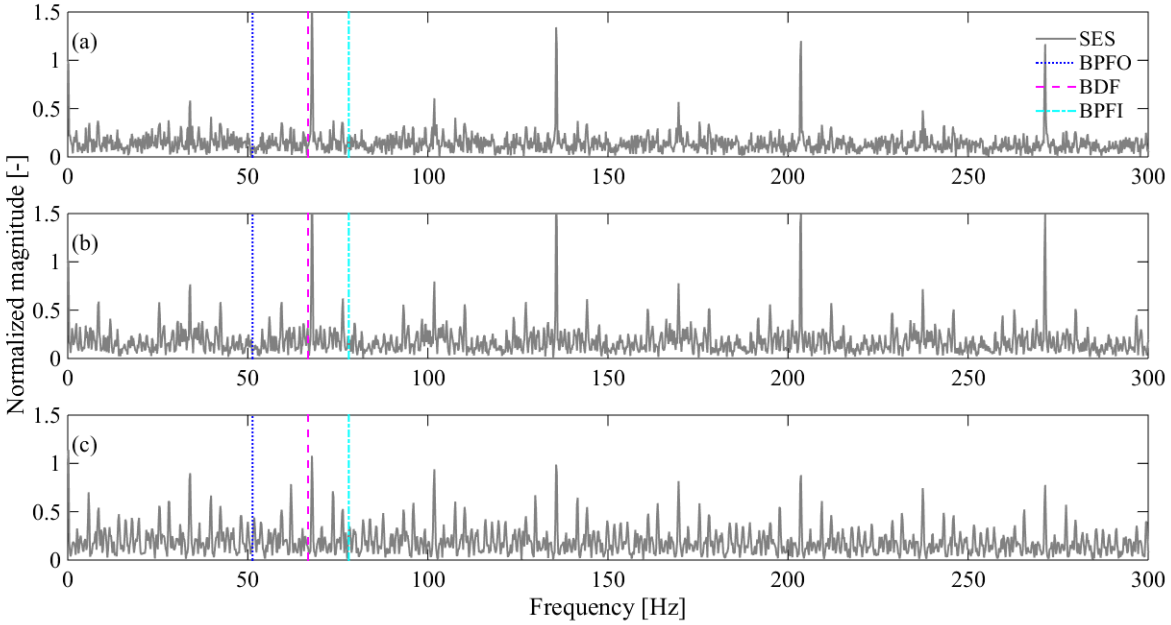

Figure 12: The squared envelope spectra (SES) obtained from the ACC signal (a), the AE signal (b) and the ACUS signal (c), in the *faulty gearbox state*, i.e. the presence of defective rolling element.

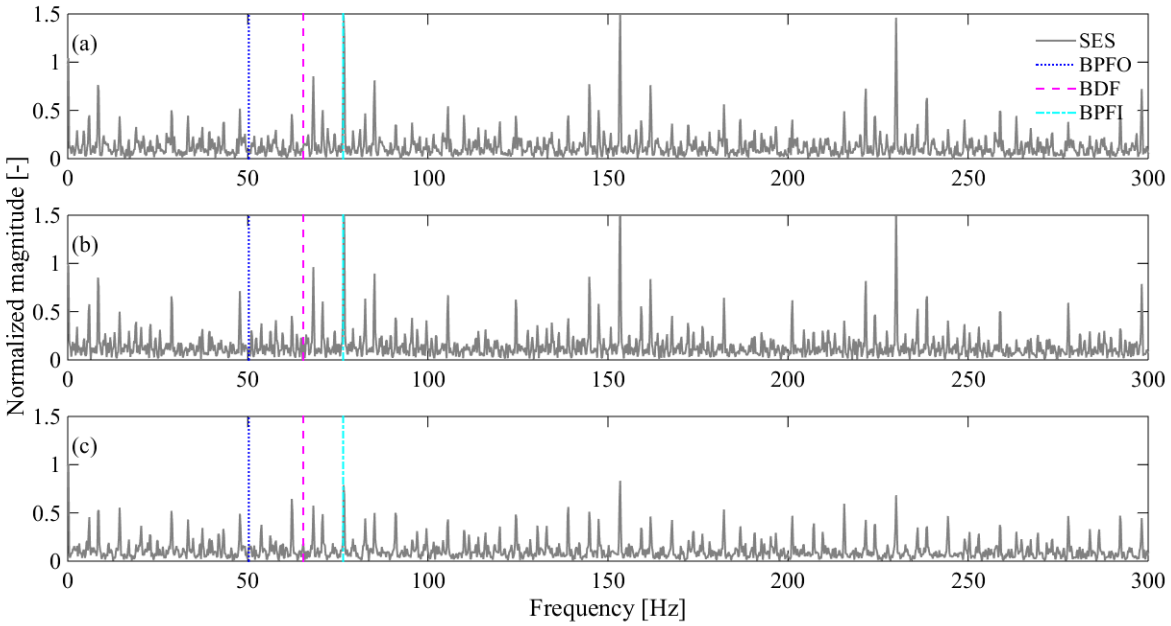

Figure 13: The squared envelope spectra (SES) obtained from the ACC signal (a), the AES signal (b) and the ACUS signal (c), in the *faulty gearbox state*, i.e. the presence of defective inner raceway.

The time-domain and frequency-domain features have been respectively calculated from the squared envelope signals and SES of all the sensors at all conditions. All the calculated time domain-features (RMS and Kurtosis) are shown in Figure 14 and Figure 15, while the calculated frequency domain features (BDF and BPFI magnitudes) are shown in Figure 16 and Figure 17.

In general, the RMS and kurtosis are sensitive to both the ball and inner race defects. This suggests that these features are not able to discriminate the two fault types. For all the sensors, it is seen that the RMS

value is prone to increase when the shaft speed increases (an exception can be seen at the shaft speed 696 rpm L2, see Figure 14). Furthermore, it is seen that the RMS feature extracted from all the sensors is consistent to separate the faulty and healthy state when the shaft speed is higher than 522 rpm. Excepting the ACUS performance in the defective inner race case, the kurtosis extracted from the envelope signals of the ACC and AES does not seem to correlate to the shaft speed for.

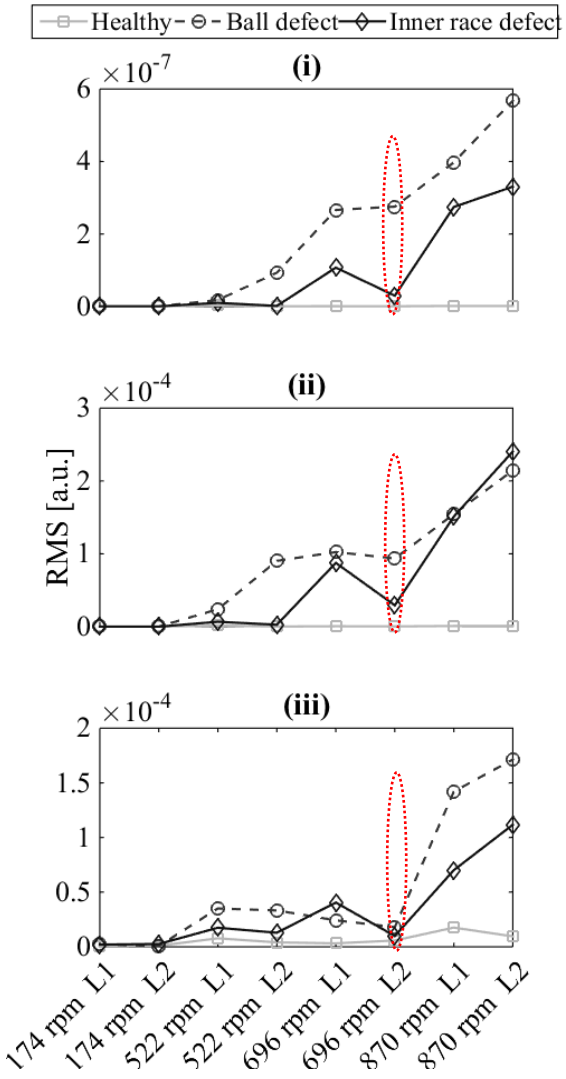

Figure 14: RMS feature extracted from the squared envelope signals of the three sensors at all the operating conditions and three different states: ACC. (i), AES (ii) and ACUS (iii).

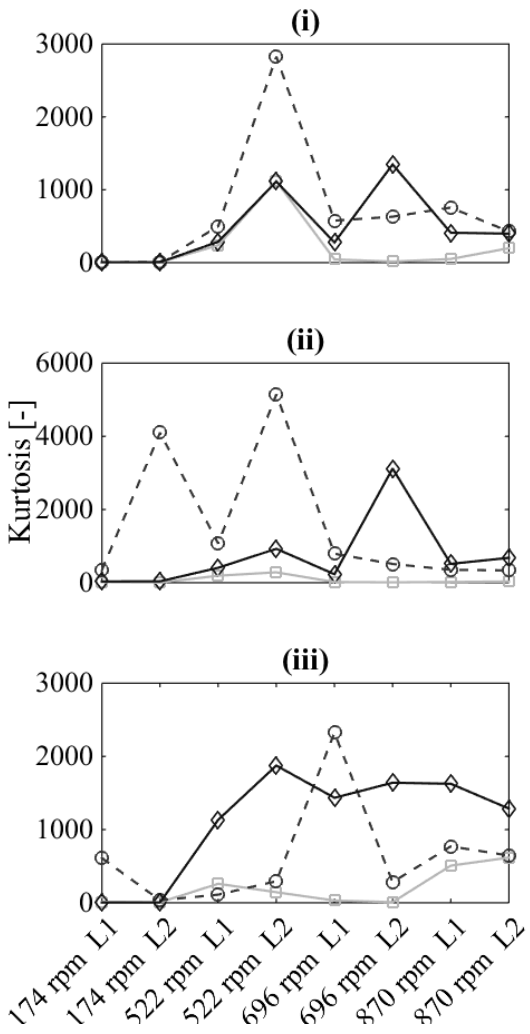

Figure 15: Kurtosis feature extracted from the squared envelope signals of the three sensors at all the operating conditions and three different states: ACC. (i), AES (ii) and ACUS (iii).

Figure 16 and Figure 17 show the frequency-domain features extracted from the SES of the three sensors. As can be seen, the BDF feature shows high value only when the rolling element fault is present, while the BPFI feature value is high only when the inner race fault is present. In general, these feature values are prone to increase when the shaft speed increases.

In the defective rolling element case, the diagnostic performance of the ACC and ACUS is quite comparable, where a clear distinction between the healthy and faulty state is observable from the shaft speed of 522 rpm onwards. However, the AES outperforms the other two sensors because a clear distinction between the healthy and faulty state is already evident at the lower shaft speed of 174 rpm L2.

The diagnostic performance of ACUS seems to be better compared to that of ACC and AES in the defective inner race case. As can be seen, the BPFI feature extracted from the ACC and AES shows a clear

distinction between the faulty and healthy state when the shaft speed is higher than 699 rpm. In contrast, the BPFI feature extracted from the ACUS is clearly distinctive from the shaft speed of 522 rpm onwards.

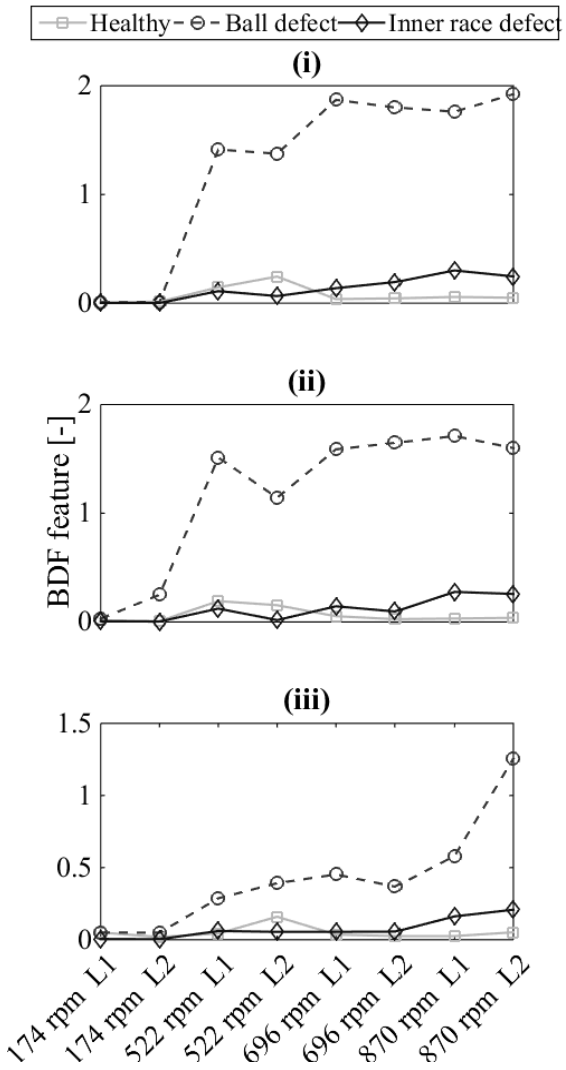

Figure 16: BDF feature extracted from the squared envelope spectra of the three sensors at all the operating conditions and three different states: ACC. (i), AES (ii) and ACUS (iii).

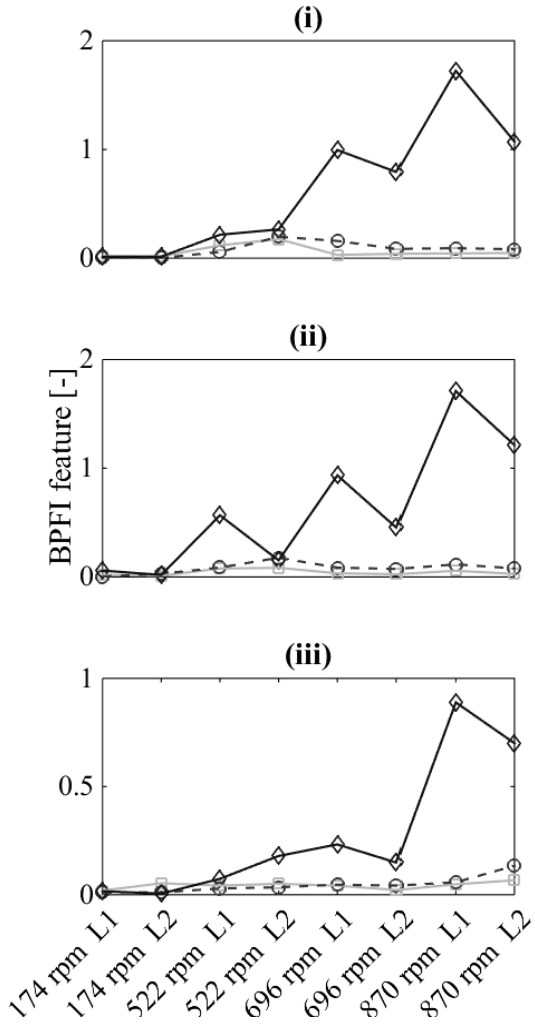

Figure 17: BPFI feature extracted from the squared envelope spectra of the three sensors at all the operating conditions and three different states: ACC. (i), AES (ii) and ACUS (iii).

6 Conclusions and outlook

A cost-effective non-contact ultrasound system (ACUS) for bearing fault diagnostics was developed and benchmarked against high-end accelerometer and acoustic emission sensor. It has been experimentally demonstrated that the diagnostics performance of ACUS is comparable with that of the high-end solutions (ICP accelerometer and Acoustic Emission sensor) for higher shaft speeds (> 500 rpm). The cost-effective ultrasound sensor can thus be used as an alternative solution for bearing fault diagnostics when contact mounting is not possible.

To further demonstrate the significances and advantages of the developed system for bearing fault diagnosis, we have identified some research directions that can be taken up in future work as follows:

- Investigation on the maximum distance between the low-cost ACUS and the bearing housing where the diagnostics performance starts to deteriorate.

- Investigation on the diagnostics performance of multiple low-cost ACUS arranged in an array and its comparison with the diagnostics performance of a standard microphone array.
- Investigation on the repeatability and stability of the feature value extracted from the low-cost ACUS signals.
- Investigation on the use of more advanced signal processing technique for possible diagnostics improvement.

Acknowledgments

Most of the materials presented in this paper were obtained during the master's thesis research of the second author. The data analysis and manuscript preparation were carried out within the frame of the *Top Competence research project of the Smart monitoring systems* research program of Flanders Make.vzw

References

[1] R. B. Randall and J. Antoni, "Rolling element bearing diagnostics - A tutorial", *Mech Syst & Sig Proc* (MSSP), 25(2), pp. 485 - 520, 2011.

[2] A. Dadouche, M.S. Safizadeh, J. Bird, W. Dmochowski, and D.S. Forsyth, "A comparative study of air-coupled ultrasound sensor and accelerometer in detecting bearing defects, In *World Tribology Congress III, Washington D.C, USA*, September 2005.

[3] A. Rezaei, A. Dadouche, V. Wickramasinghe, and W. Dmochowski, "A comparison study between acoustic sensors for bearing fault detection under different speed and load using a variety of signal processing techniques", *Tribology Transactions*, 54(2), pp. 179-186, 2011.

[4] LM386 Low Voltage Audio Power Amplifier, taken from Texas Instruments, August 2000 (http://www.ti.com/lit/ds/symlink/lm386.pdf).

[5] J. Shiroishi, Y. Li, S. Liang, T. Kurfess and S. Danyluk, "Bearing condition diagnostics via vibration and acoustic emission measurements", *Mech Syst & Sig Proc* (MSSP), 11(5), pp. 693 - 705, 1997.

[6] J. Antoni, "Fast computation of the kurtogram for the detection of transient faults", *Mech Syst & Sig Proc* (MSSP), 21(1), pp. 108 - 124, 2007.